Decoupling Land Surface Effects from CO_2 Effective Radiative Forcing in a Climate Model

BOSONG ZHANG,[a] BRIAN J. SODEN,[b] HAOZHE HE,[c] AND RYAN J. KRAMER[d]

[a] *Program in Atmospheric and Oceanic Sciences, Princeton University, Princeton, New Jersey*
[b] *Rosenstiel School of Marine, Atmospheric and Earth Science, University of Miami, Miami, Florida*
[c] *High Meadows Environmental Institute, Princeton University, Princeton, New Jersey*
[d] *NOAA/GFDL, Princeton, New Jersey*

(Manuscript received 23 April 2025, in final form 28 July 2025, accepted 3 September 2025)

ABSTRACT: Accurate estimation of effective radiative forcing (ERF) is essential for understanding climate responses to external forcing. A common approach involves simulations with fixed sea surface temperatures (SSTs) while allowing land temperatures to evolve freely. However, this setup can introduce land-induced adjustments that influence ERF estimates. Using a state-of-the-art climate model, we investigate the influence of land surface temperature changes in shaping ERF under an abrupt quadrupling of carbon dioxide (CO_2) ($4xCO_2$). We conduct a series of experiments where land temperatures and soil moisture are either interactive or prescribed to their climatological values. We find that fixing land temperatures and soil moisture increases $4xCO_2$ ERF from 8.26 to 9.78 W m^{-2}, primarily due to reduced longwave cooling and cloud changes. Additional idealized experiments demonstrate a monotonic decrease in $4xCO_2$ ERF but enhanced land precipitation with increasing land warming but fixed SSTs. These findings highlight the critical role of land processes in shaping radiative forcing estimates and provide insights into how land–sea warming contrasts influence convection, moisture transport, and precipitation patterns.

SIGNIFICANCE STATEMENT: Effective radiative forcing (ERF) is a fundamental metric for understanding how agents like carbon dioxide (CO_2) perturb Earth's energy balance. A widely used method estimates CO_2 ERF by fixing sea surface temperatures while allowing land temperatures to respond in atmosphere–land coupled models. However, this approach involves land-induced responses, as land warming influences atmospheric energy exchanges in complex ways. Using an atmosphere–land coupled model, we show that suppressing land temperature changes amplifies the estimated CO_2 ERF. Idealized experiments further reveal that ERF decreases consistently as land warms. These findings underscore the importance of representing land surface processes when quantifying radiative forcing and highlight the critical role of land–atmosphere interactions in shaping climate response.

KEYWORDS: Atmosphere-land interaction; Feedback; Radiative forcing; Climate models

1. Introduction

Evaluating changes in the mean state of the climate system often follows a forcing–feedback framework, where the net radiation at the top of the atmosphere (TOA) and the mean surface temperature are key variables of interest. For annual-mean and global-mean values, when net radiation at the TOA is close to zero, the system is in near equilibrium, and the contemporary mean surface temperature remains stable. However, when an external forcing—such as an increase in carbon dioxide (CO_2) concentration—is applied, the climate system must respond. This relationship is commonly expressed as

$$N = F + \lambda \Delta T, \tag{1}$$

where N is the net radiation at TOA, F is the radiative forcing, ΔT is the surface air temperature change, and λ is the climate feedback parameter. By this convention, a positive λ indicates positive feedback, leading to additional energy accumulation in the climate system, whereas a negative λ means negative feedback that reduces energy. If F and λ are well estimated, the global-mean surface air temperature change ΔT can be determined once the climate system returns to near equilibrium (when $N \approx 0$).

A widely used approach to estimate equilibrium ΔT is the linear, zero-dimensional energy balance model proposed by Gregory et al. (2004). While the Gregory method is straightforward, numerous studies have shown that estimating the climate feedback parameter λ is more complex than initially assumed. One key challenge is the influence of the spatial pattern of sea surface temperature (SST) changes on λ (Andrews et al. 2022; Gregory and Andrews 2016; Guillaume-Castel and Meyssignac 2025; Stevens et al. 2016). This so-called "SST pattern effect" has been investigated through SST perturbation experiments using atmospheric general circulation models (Alessi and Rugenstein 2023; Bloch-Johnson et al. 2024; Dong et al. 2019; Hsieh et al. 2024; Quan et al. 2024, 2025; Wang et al. 2025;

Supplemental information related to this paper is available at the Journals Online website: https://doi.org/10.1175/JCLI-D-25-0231.s1.

Corresponding author: Bosong Zhang, bosongzhang@gmail.com

DOI: 10.1175/JCLI-D-25-0231.1

TABLE 1. A list of experiments conducted.

Experiment ID	CO_2 level	Land temperature	Soil moisture (liquid and ice; top three soil levels)	Stomatal response to CO_2
A1	1xCO_2	Interactive	Interactive	—
A2	4xCO_2	Interactive	Interactive	Yes
A2_rad	4xCO_2	Interactive	Interactive	No
B1	1xCO_2	Prescribed using climatological values from control (A1)	Interactive	—
B2	4xCO_2	Prescribed using climatological values from control (A1)	Interactive	Yes
B2_rad	4xCO_2	Prescribed using climatological values from control (A1)	Interactive	No
C1	1xCO_2	Prescribed using climatological values from control (A1)	Prescribed using climatological values from control (A1)	—
C2	4xCO_2	Prescribed using climatological values from control (A1)	Prescribed using climatological values from control (A1)	Yes
C2_rad	4xCO_2	Prescribed using climatological values from control (A1)	Prescribed using climatological values from control (A1)	No

Williams et al. 2023; Zhang et al. 2023a; Zhou et al. 2017). However, these experiments inevitably involve changes in land surface temperatures, which also influence λ. Recent observational analyses suggest that land temperature change tends to exert a negative contribution to λ, emphasizing the importance of including land surface effects when interpreting the pattern effect (Thompson et al. 2025). Just as the SST pattern can modify λ, the spatial distribution of radiative forcing F can affect λ through the associated patterns of surface temperature response (Haugstad et al. 2017; Myhre et al. 2024; Salvi et al. 2023; Zhang et al. 2023b).

Considerable research has also focused on the definition and interpretation of radiative forcing. While instantaneous radiative forcing provides one measure, effective radiative forcing (ERF), which includes rapid atmospheric adjustments (e.g., changes in temperature, water vapor, surface albedo, and clouds) with surface temperature held fixed, offers a more comprehensive view of the forcing relevant to climate response (Forster et al. 2016; Myhre et al. 2013; Ramaswamy et al. 2019; Sherwood et al. 2015). However, ERF is typically assessed using model simulations where SSTs are fixed but land temperatures are free to respond. Several studies have attempted to account for radiative responses to land temperature changes when calculating ERF. These corrections include estimates based on a model's long-term feedback parameter (Hansen et al. 2005) and the use of radiative kernels (Smith et al. 2020b; Tang et al. 2019). However, as noted by Andrews et al. (2021), these methods have not been systematically compared against direct model calculations of ERF in which both SST and land surface temperatures are fixed. Andrews et al. (2021) evaluated ERF using a modeling framework in which surface temperatures over both land and ocean were prescribed, following approaches described in Ackerley and Dommenget (2016) and Ackerley et al. (2018). Their findings suggest that the radiative effects of land warming may be model dependent due to intermodel differences in land surface physics and the specific methods used to prescribe land properties.

Motivated by their results, this study evaluates ERF using a different climate model with prescribed land temperatures. Specifically, we implement a fixed-land-temperature approach in the NOAA Geophysical Fluid Dynamics Laboratory (GFDL) atmospheric model, version 4 (AM4), introduced briefly in section 2. While our methodology largely follows that of Andrews et al. (2021), we introduce modifications tailored to AM4. This setup enables us to compute ERF using both fixed-SST and fixed-surface-temperature experimental designs, providing a direct quantification of the radiative effects and adjustments associated with land temperature changes in the commonly used fixed-SST ERF framework. While our analysis primarily focuses on the response to a quadrupling of CO_2, we also examine how the magnitude of land warming influences the broader climate response. Results are presented in section 3, with a summary and discussion in section 4.

2. Methods

a. Model and experiments

In this study, we use the GFDL AM4 (Zhao et al. 2018a,b) to perform numerical experiments. AM4 employs a cubed-sphere grid with 96 × 96 grid cells per face, corresponding to an approximate horizontal resolution of 100 km. The postprocessed model output is regridded to a latitude–longitude grid with 180 grid points in the meridional direction and 288 points in the zonal direction, yielding a horizontal resolution of 1.0° latitude × 1.25° longitude.

The control simulation is forced by observed climatological monthly mean SSTs and sea ice fractions averaged from 1981 to 2014, while land temperatures are allowed to evolve freely. Vegetation is prescribed as static. Forcing levels, such as greenhouse gas concentrations and aerosol emissions, are held constant at year 2010 values, with the CO_2 concentration set to 387.5 ppm. This experiment is referred to as the control and labeled A1.

We also conduct an abrupt quadrupling of CO_2 experiment, in which the atmospheric CO_2 concentration is increased to

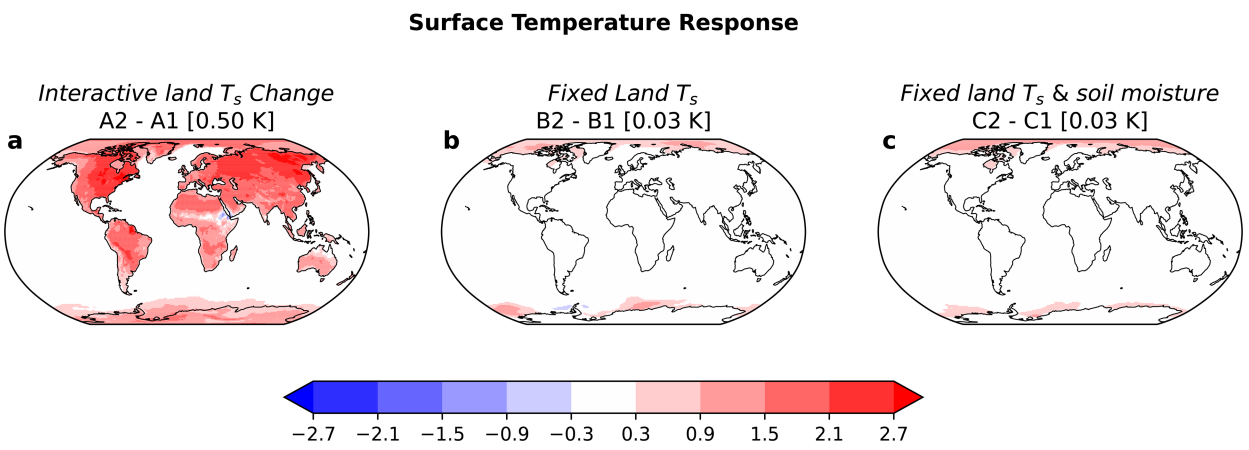

FIG. 1. Change in surface temperature for (a) A2–A1, (b) B2–B1, and (c) C2–C1.

1550.0 ppm and held fixed. Although vegetation remains static, the stomatal response to elevated CO_2 is included via a parameter that modulates photosynthesis. This setup allows stomatal conductance to respond to elevated CO_2 without affecting vegetation growth. All other experimental conditions in the abrupt quadrupling of CO_2 experiment are identical to those in A1. This experiment is referred to as 4xCO_2 and labeled A2. In A1 and A2, adhering to traditional fixed-SST protocols (e.g., Myhre et al. 2017; Pincus et al. 2016), state variables from the land model are interactive, meaning that land temperatures and other land-related variables in the 4xCO_2 experiment can freely respond to the abrupt CO_2 increase. Each simulation runs for 31 years, with the first year treated as spinup and the final 30 years used for the analysis. All subsequent experiments follow the same simulation length.

To investigate the role of land surface temperature responses in modulating ERF, we save land surface temperature (including canopy-air temperature and radiative surface temperature) and soil moisture (including soil ice and soil liquid) at a 3-h frequency from both A1 and A2. This frequency preserves the diurnal cycle and allows prescribed-temperature experiments to realistically capture the daily evolution of land temperatures driven by solar radiation. Using data from the last 30 years, we compute climatological values that will be used in fixed-land-style experiments described later. The canopy-air temperature and radiative surface temperature are single-level variables, while soil ice and soil liquid are multilevel variables. We save data from the top three soil layers, located at depths of 0.01, 0.04, and 0.08 m below the land surface.

As shown in Andrews et al. (2021), land surface temperature and soil moisture are both prescribed. We conduct a sequence of fixed-surface experiments using AM4. First, we prescribe only land surface temperature (experiments B1 and B2 in Table 1), while allowing soil moisture to remain interactive—analogous to the fixed-SST protocol over oceans. Temperatures are prescribed globally over land, including ice sheets (e.g., Greenland, Antarctica), but not over sea ice. We also test an alternative approach by prescribing subsurface soil temperature but find it ineffective in constraining surface warming. To further isolate land effects, we perform additional experiments (see C1 and C2 in Table 1) where both land temperature and soil moisture (top three levels at 0.01-, 0.04-, and 0.08-m depths) are prescribed using multiyear climatology from A1. This setup closely mirrors that of Andrews et al. (2021), where both quantities are fixed to eliminate

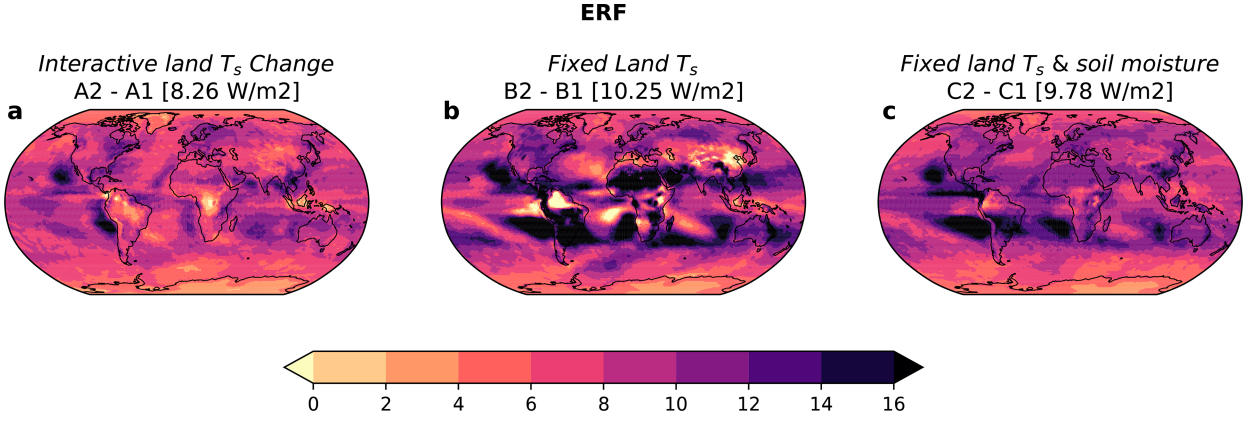

FIG. 2. As in Fig. 1, but for change in net TOA radiation (i.e., the definition of ERF).

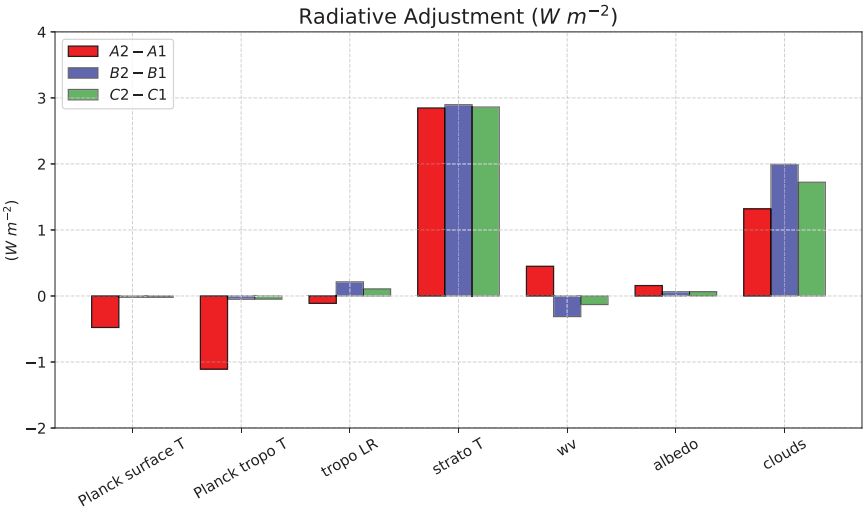

FIG. 3. Comparison of the global-mean radiative adjustments in the different ERF experimental designs. (left–right) Radiative adjustment from surface Planck temperature, tropospheric Planck temperature, lapse rate, stratospheric temperature, water vapor, surface albedo, and cloud.

land surface adjustments. To summarize, the additional experiments are

B1: like the control run (A1), with the same CO_2 concentration. However, in B1, land surface temperatures are prescribed using climatological values from A1.
B2: identical to B1, except that CO_2 is quadrupled. Land surface temperatures in B2 are also prescribed using climatological values from A1.
C1: like the control run (A1), with the same CO_2 concentration. However, in C1, land surface temperatures, soil ice, and soil liquid at the top three model levels are prescribed using climatological values from A1.
C2: same as C1, except that CO_2 is quadrupled.

The comparison between A1 and A2 aims at evaluating the traditional way of calculating ERF, while the comparison between B1 and B2 is to investigate the ERF without the effects of land warming. The comparison between C2 and C1 reduces the freedom of soil moisture, which is more similar to the setup done by Andrews et al. (2021), where soil moisture is prescribed together with land temperature in their experiment design. In A2, B2, and C2, vegetation responds to elevated CO_2 via stomatal conductance. To isolate this physiological effect, we also perform additional experiments (denoted "_rad") in which the CO_2 concentration used in photosynthesis is fixed at control values, thereby disabling the stomatal response, as in Andrews et al. (2021). A list of the experiments is shown in Table 1.

b. *Effective radiative forcing, radiative kernels, and adjustments*

As defined in previous studies (Andrews et al. 2021; Forster et al. 2016; Myhre et al. 2013; Smith et al. 2018), ERF is computed as the change in the net TOA radiative flux due to a perturbation in a forcing agent like CO_2, relative to the control state. This is the way of how ERF is calculated in this study. Unlike instantaneous radiative forcing (IRF), ERF accounts for rapid adjustments and can be written by the equation shown in Andrews et al. (2021):

$$\mathrm{ERF} = \mathrm{IRF} + A_{\mathrm{Planck_{surf}}} + A_{\mathrm{Planck_{trop}}} + A_{\mathrm{LR}} + A_{\mathrm{strat}} + A_q + A_\alpha + A_c + \epsilon.$$

Note that this equation includes a surface Planck adjustment term, $A_{\mathrm{Planck_{surf}}}$, which reflects the contribution from surface temperature changes (usually from land surface). In this study, our goal is to minimize this contribution as much as possible—that is, to quantify ERF under conditions where surface temperature remains fixed everywhere.

We employ the radiative kernel technique following Soden et al. (2008) to compute the radiative adjustment processes on the right-hand side of the equation. The radiative kernels used in this study are based on the atmospheric component of a recent generation climate model (HadGEM3) developed by the U.K. Met Office (Smith et al. 2020a). This method decomposes the response of radiative fluxes at the TOA into individual components caused by changes in surface temperature $A_{\mathrm{Planck_{surf}}}$, a vertically uniform tropospheric temperature change $A_{\mathrm{Planck_{trop}}}$, tropospheric lapse rate A_{LR}, stratospheric temperature A_{strat}, water vapor A_q, surface albedo A_α, and cloud A_c. Soden et al. (2008) showed that cloud adjustment can be diagnosed from the response of cloud radiative effect corrected by the cloud-masking effect. More details of the calculation of A_c can be found in Smith et al. (2018). The term ϵ represents a residual.

3. Results

a. *Impact of land surface temperatures*

Before assessing the role of fixing land temperatures and soil moisture on ERF, we note that the baseline climatology

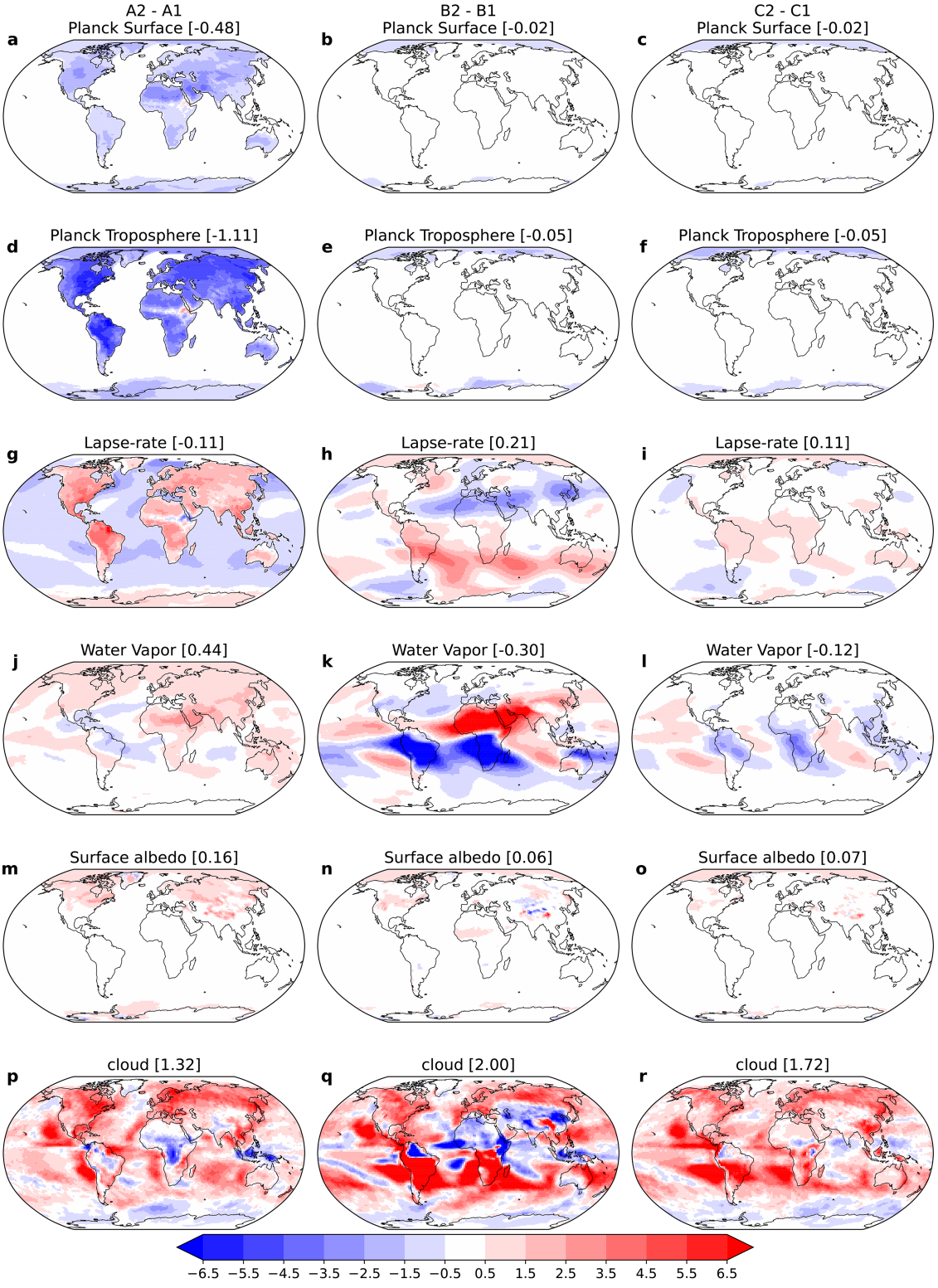

FIG. 4. Maps of radiative adjustments for (left) A2–A1, (middle) B2–B1, and (right) C2–C1. (top–bottom) Adjustment from surface Planck, tropospheric Planck, lapse rate, water vapor, surface albedo, and cloud responses.

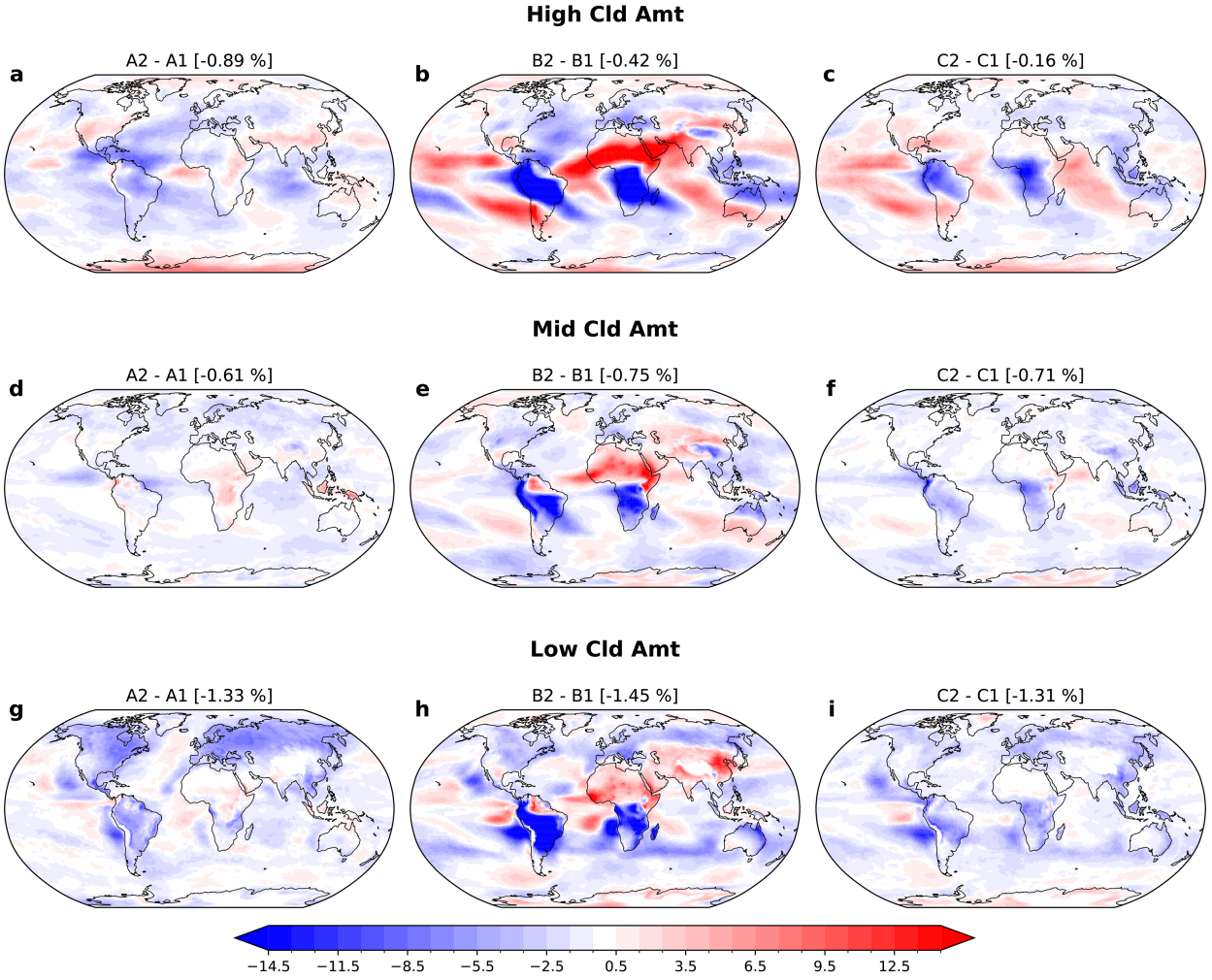

FIG. 5. Change in high-level, midlevel, and low-level cloud amount for (left) A2–A1, (middle) B2–B1, and (right) C2–C1.

across A1, B1, and C1 is nearly identical (not shown), indicating that the use of prescribed climatological values does not alter the model's base state. This provides a consistent foundation for interpreting the differences in surface temperature responses under elevated CO_2.

Figure 1 shows the surface temperature change from $1xCO_2$ to $4xCO_2$ across different experimental configurations. In the default model setup where land processes are interactive, A2–A1 exhibits significant land warming, particularly over North America, Europe, Asia, and North Africa, while Southern Hemisphere land regions exhibit relatively smaller warming (Fig. 1a). By contrast, when the canopy-air and radiative surface temperatures are prescribed (B2–B1), surface temperature changes are near zero over land by design, with the only exceptions occurring over sea ice regions (Fig. 1b). Similarly, the C2–C1 configuration (Fig. 1c), which additionally prescribes soil moisture, produces a surface temperature response that closely mirrors that of B2–B1.

Figure 2 shows the ERF due to changes in CO_2 concentration. In the default setup with interactive land processes, ERF in A2–A1 is 8.26 W m^{-2}. When both the canopy-air temperature and radiative surface temperature are prescribed in the land model, ERF increases to 10.25 W m^{-2} in B2–B1. When soil moisture is additionally prescribed on top of the fixed land surface temperature, ERF is 9.78 W m^{-2} in C2–C1. This latter configuration, in which both soil moisture and land temperature are prescribed, aligns with the experimental design of Andrews et al. (2021), making the increase in ERF from 8.26 to 9.78 W m^{-2} a more appropriate comparison. The difference between C2–C1 and A2–A1 is 1.52 W m^{-2} (~18% increase), greater than 0.95 W m^{-2} by the model used in Andrews et al. (2021).

The larger ERF in B2–B1 may be attributed to changes in soil moisture, as B1 and B2 prescribe only land surface temperature while allowing soil moisture to evolve freely. In the default setup (A2–A1), there is a substantial reduction in soil ice over Northern Hemisphere continents with land warming, whereas changes over Southern Hemisphere continents are minimal (Fig. S1 in the online supplemental material). This reduction diminishes largely in B2–B1, suggesting the influence of prescribed land temperature. However, soil liquid

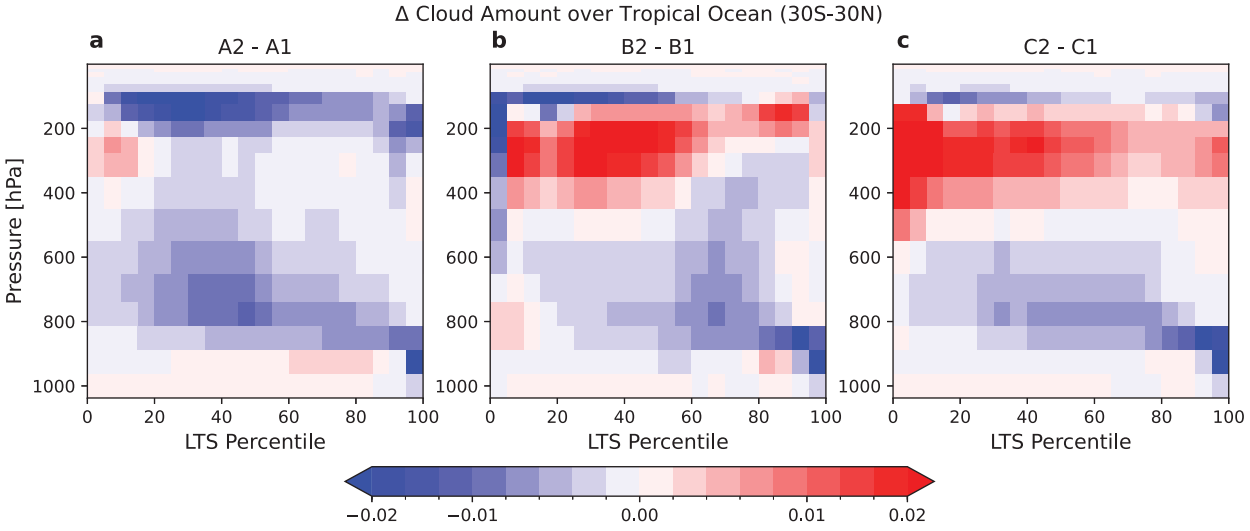

FIG. 6. Cloud amount change computed from monthly mean tropical ocean profiles sorted by LTS for (a) A2–A1, (b) B2–B1, and (c) C2–C1.

exhibits more pronounced and spatially diverse responses in B2–B1 than in A2–A1 (Fig. S2): Elevated CO_2 causes strong reductions in soil liquid over South America, South Africa, and North Australia, while increases are observed over North Africa and much of Asia. These changes are associated with shifts in precipitation and evaporation (not shown). However, they may be artifacts and thus physically unrealistic.

Given these limitations, the C2–C1 configuration—where both land temperature and soil moisture are fixed—offers a more robust assessment of ERF and is consistent with the approach of Andrews et al. (2021). Nonetheless, documenting the B2–B1 case remains valuable for understanding the influence of soil moisture feedbacks under partially fixed land conditions. Although we do not have a sound explanation for the soil moisture change in B2–B1, it can be explored in future studies. With this in mind, we focus the following comparison between A2–A1 and C2–C1 but retain results from B2–B1.

We further use radiative kernels to analyze radiative adjustment processes across each pair of simulations. Figure 3 shows global-mean values of individual adjustments. In the default setup with interactive land processes (A2–A1; red bars), the Planck adjustments (including surface and tropospheric components) are negative. The lapse rate adjustment is slightly negative while adjustments from stratospheric temperature, water vapor, surface albedo, and clouds are positive, consistent with standard CO_2 perturbation fixed-SST experiments from Andrews et al. (2021) and the CMIP6 multimodel mean values (Smith et al. 2020b). With prescribed land surface temperature and soil moisture, the Planck adjustments become negligible as expected. The stratospheric temperature adjustment remains almost unchanged. The lapse rate adjustment becomes slightly positive. The water vapor and surface albedo adjustments decrease, but the cloud adjustment increases (C2–C1; green bars). Not only is the overall land

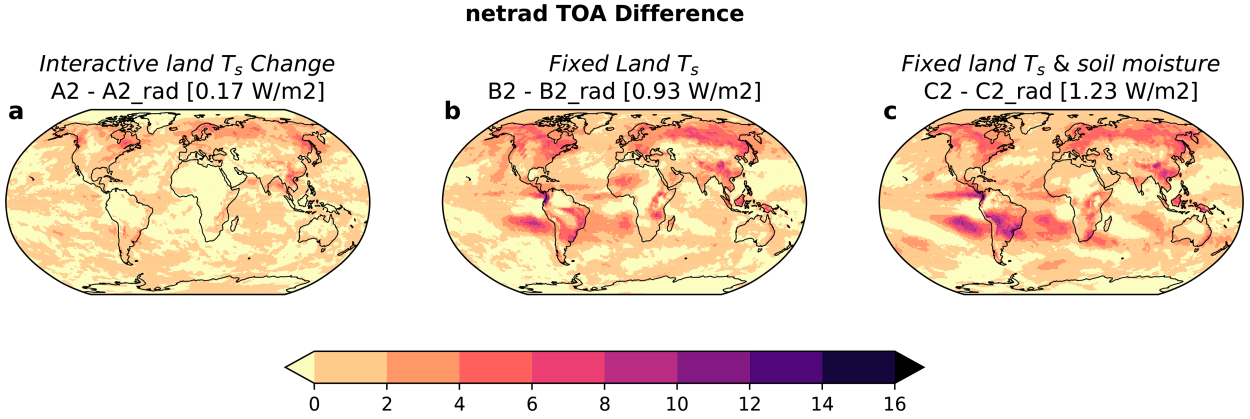

FIG. 7. Change in net radiation at TOA for (a) A2–A2_rad, (b) B2–B2_rad, and (c) C2–C2_rad.

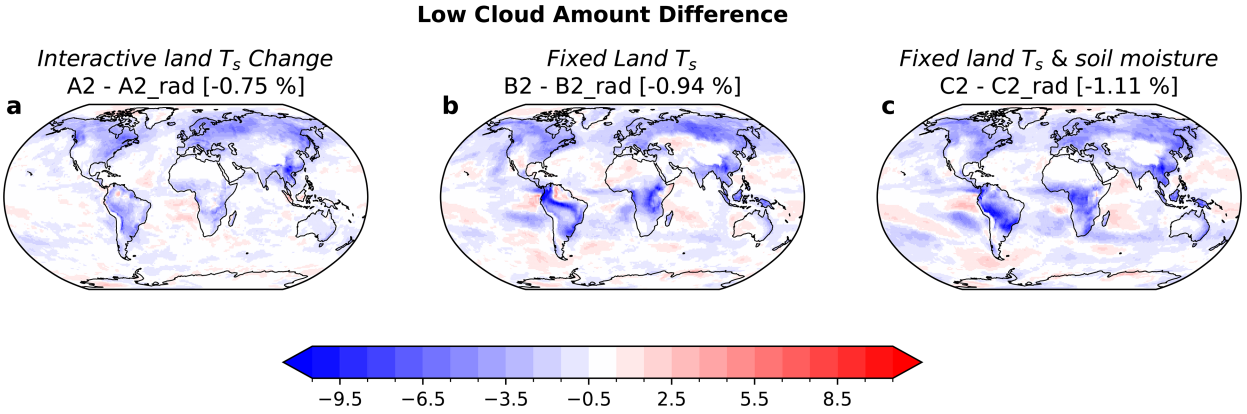

FIG. 8. Change in low cloud amount for (a) A2–A2_rad, (b) B2–B2_rad, and (c) C2–C2_rad.

effect consistent with Andrews et al. (2021), but the behavior of individual adjustments computed using radiative kernels also generally agrees in both sign and magnitude. This consistency extends to alternative land-effect correction methods, such as those presented by Tang et al. (2019).

Figure 4 shows the spatial distribution of radiative adjustment processes. By experiment design, the Planck adjustments for B2–B1 and C2–C1 are zero over land regions. Andrews et al. (2021) found that the lapse rate adjustment shifts from near zero to negative with prescribed land processes. In AM4, the lapse rate adjustment becomes slightly positive with fixed surface temperature and soil moisture in C2–C1 (Fig. 4i). Radiative adjustments associated with water vapor and surface albedo in AM4 decrease with fixed land surface temperatures, qualitatively consistent with the results shown by Andrews et al. (2021).

Despite the global-mean cloud adjustment increases with fixed land surface temperature in this study and in Andrews et al. (2021), substantial spatial differences emerge between the two models. When land warming is included (A2–A1), the positive cloud adjustment in AM4 is primarily driven by positive values over both ocean and land, whereas in Andrews et al. (2021), it originates mainly from land. Over tropical marine stratocumulus regions, Andrews et al. (2021) showed a negative cloud adjustment (see their Fig. 3p), whereas AM4 exhibits a positive cloud adjustment over these regions (Fig. 4p). These opposing cloud adjustments align with differences in cloud amount changes between the two models, particularly in low-level cloud amount (see their Fig. 5 and Fig. 5 in this study). In Andrews et al. (2021), suppressing land warming was found to reduce the negative cloud adjustment over marine stratocumulus regions (their Figs. 3p,q). In contrast, the comparison between A2–A1 (Fig. 4p) and C2–C1 (Fig. 4r) does not indicate a robust impact of prescribing land properties on the positive cloud adjustment in these regions.

To better understand AM4's distinct cloud response, we examine the vertical profile of cloud amount change over tropical oceans. The cloud amount is binned by lower-tropospheric stability (LTS), defined as the difference between potential temperature at 700 hPa and the SST, as in Wyant et al. (2012). We find a reduction in cloud amount from about 600 to 900 hPa but a slight increase near the surface for the top 50% LTS percentiles (Fig. 6), which implies a shallowing of the marine boundary layer with elevated CO_2 concentration. Similar cloud changes in response to increasing CO_2 have been reported in Wyant et al. (2012) in a superparameterized climate model (see their Figs. 9b and 11d). Nevertheless, it is important to note that AM4's simulated mean climatological amount of tropical marine stratocumulus has known biases compared to observations (Zhao et al. 2018a). In addition, we notice an overall increase in high cloud fraction over tropical ocean in C2–C1 (Figs. 5c and 6c). A detailed investigation of the high cloud responses is beyond the scope of this study and thus leaves to future research.

b. *Role of stomatal response*

As shown by Doutriaux-Boucher et al. (2009), the physiological effect of CO_2 on plant stomatal conductance can influence land surface warming, low cloud cover, and consequently, estimates of ERF. Here, we briefly assess the impact of elevated CO_2 on stomatal conductance in our experiments. The standard experiments (A2, B2, and C2) include this physiological response. To isolate its effect, we perform additional experiments

TABLE 2. A list of the experiments to test the sensitivity to the magnitude of land warming.

Experiment ID	CO_2 level	Land temperature
C1	1xCO_2	Prescribed using climatological values from control
C2	4xCO_2	Prescribed using climatological values from control
C3_half	4xCO_2	Prescribed using climatological values from control plus half of the difference between A2 and A1
C3	4xCO_2	Prescribed using climatological values from 4xCO_2
C3_double	4xCO_2	Prescribed using climatological values from control plus doubling of the difference between A2 and A1

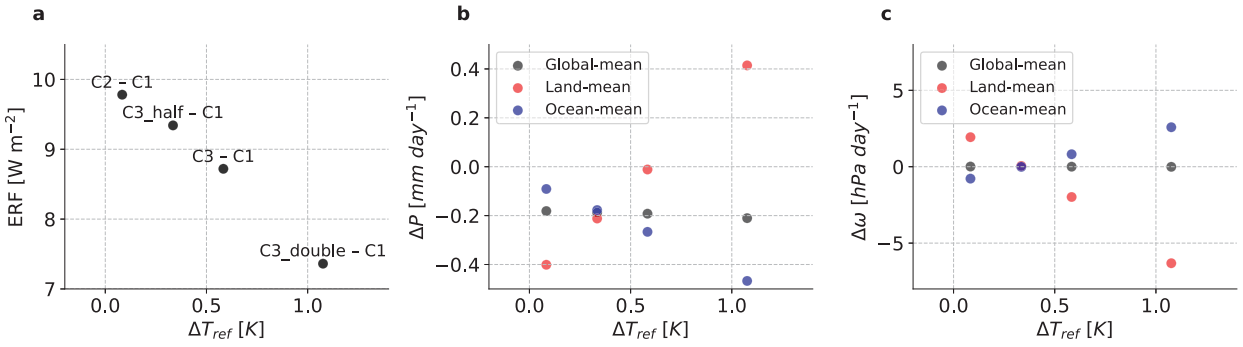

FIG. 9. Scatterplots of surface air temperature changes vs (a) ERF; (b) changes in globally, land-averaged, and ocean-averaged precipitation; and (c) changes in globally, land-averaged, and ocean-averaged pressure velocity at 500 hPa. In (b) and (c), the data points from left to right represent C2–C1, C3_half–C1, C3–C1, and C3_double–C1, respectively, with labels omitted for a clear presentation.

in which photosynthesis does not respond to elevated CO_2—achieved by modifying a single parameter in AM4. These experiments are denoted with the "_rad" suffix (Table 1), consistent with the _rad configuration used in Andrews et al. (2021).

Figure 7 shows the change in net TOA radiation due to the stomatal effect. In A2–A2_rad, the ERF contribution from stomatal conductance is 0.17 W m^{-2}, comparable to 0.24 W m^{-2} reported by Andrews et al. (2021). In C2–C2_rad, the stomatal effect increases to 1.23 W m^{-2}, which is slightly larger than 0.79 W m^{-2} found in Andrews et al. (2021) under fixed-land-surface conditions. This enhanced forcing is closely linked to changes in low cloud amount (Fig. 8). Specifically, A2–A2_rad shows a 0.75% global-mean decrease in low cloud cover, whereas C2–C2_rad exhibits a larger decrease of 1.11%.

c. *Sensitivity to the degree of land warming*

Another key question is how sensitive ERF and other climate system components are to the magnitude of land warming. Since land has a much lower heat capacity than the ocean, it adjusts more rapidly to external forcing. However, the extent of land warming and the land–sea warming contrast remain highly uncertain. To explore this sensitivity, we conducted additional idealized experiments by varying the degree of land warming. Specifically, C3–C1 represents the land warming induced by 4xCO_2 relative to the control climate. We then designed two additional experiments: one where land warming is halved (C3_half) and another where it is doubled (C3_double), as detailed in Table 2. Maps of change in surface air temperature can be found in Fig. S3.

Our results show that ERF decreases as land warming increases (Fig. 9a). However, global-mean precipitation does not exhibit a clear trend. Instead, the primary response is a spatial redistribution of precipitation: increases over land and decreases over the ocean (Fig. 9b), accompanied by enhanced upward motion over land and suppressed ascent over the ocean (Fig. 9c). Figure 10 shows zonal-mean, global, land-averaged, and ocean-averaged precipitation changes. Maps of precipitation changes across these comparisons are provided in Fig. S4. This shift in mean precipitation aligns with previous findings (Chadwick et al. 2019; Wyant et al. 2012), suggesting that amplified land–sea warming contrast tends to enhance upward motions and precipitation over land.

These findings also raise important considerations for other forcing agents, particularly aerosols. Given the overall negative sign of aerosol ERF and the spatial pattern of aerosol–cloud interactions, ERF due to aerosols may be even more sensitive to land surface temperature adjustments. This is

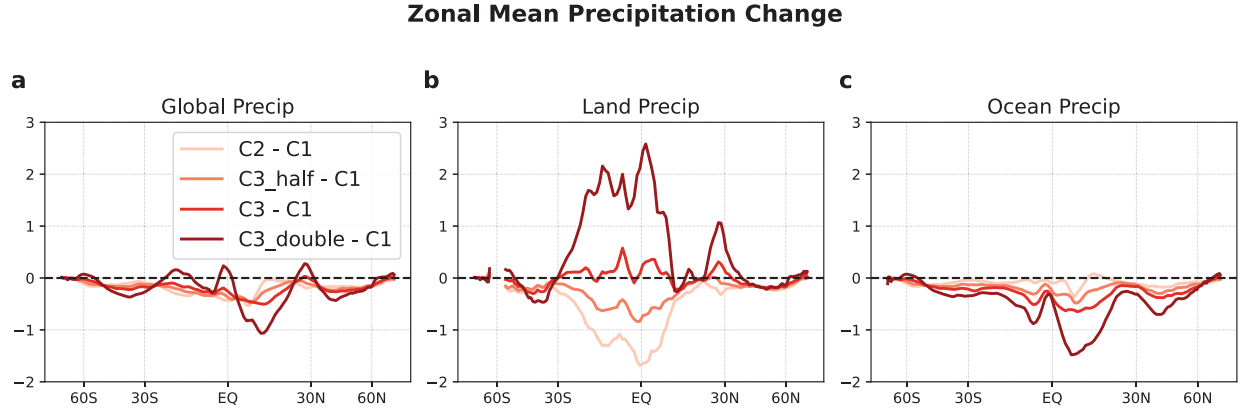

FIG. 10. Change in zonal-mean precipitation over (a) global, (b) land, and (c) ocean for C2–C1, C3_half–C1, C3–C1, and C3_double–C1.

especially relevant because major aerosol forcing sources are located over or near land regions (Koch et al. 2007), where land–atmosphere coupling plays a critical role. We therefore recommend that future studies extend the fixed-land-temperature framework to aerosol perturbation experiments to evaluate the extent to which land surface adjustments influence aerosol ERF, land temperature, and precipitation. This sensitivity likely warrants special attention in model intercomparison and forcing attribution studies.

4. Summary and discussion

In this study, we investigate the role of land surface responses in estimating effective radiative forcing (ERF) using AM4, an atmospheric model developed at NOAA's GFDL. A common method for estimating ERF involves simulations with fixed sea surface temperatures (SSTs) while allowing land processes to respond to external forcing. However, because land conditions are not held constant, the resulting land responses may introduce adjustments that complicate the interpretation of ERF. To address this, we prescribe land surface conditions when estimating the ERF of an abrupt quadrupling of CO_2.

To isolate the effect of land surface temperature changes, we conduct a series of AM4 experiments. In the default fixed-SST configuration, where land temperatures are interactive, the ERF (A2–A1) is 8.26 W m^{-2}. When land surface temperature is prescribed (B2–B1), ERF increases to 10.25 W m^{-2}; however, this configuration introduces physically unrealistic changes in soil moisture and associated cloud responses. To remove this artifact, we additionally fix soil moisture (C2–C1), resulting in an ERF of 9.78 W m^{-2}. The radiative kernel analysis reveals that land warming primarily enhances longwave radiative cooling through increased surface and atmospheric emission. Conversely, when both land temperature and soil moisture are fixed, this longwave cooling is largely removed, though this is partially offset by an increase in cloud adjustment. These findings are consistent with Andrews et al. (2021), who found similar land-induced effects using a coarser-resolution model. We also assess the physiological (stomatal) response of vegetation to elevated CO_2. In AM4, disabling this effect leads to a slight reduction in ERF, primarily due to changes in low cloud amount, consistent with prior studies (Andrews et al. 2021; Doutriaux-Boucher et al. 2009).

Because land responds to radiative forcing more rapidly than the ocean, initial warming is concentrated over land. This amplifies the land–sea warming contrast and alters convective activity, moisture transport, and precipitation patterns. To explore the influence of land warming on ERF, we conduct a series of idealized experiments and find a monotonic decrease in ERF with increasing land temperature. This result is expected, as the Planck response—a dominant component of radiative adjustment—scales approximately linearly with temperature. Variations in land warming may also affect extreme events such as tropical cyclones, heat waves, droughts, and floods, underscoring the need for further investigation.

While efforts to fix land surface temperatures have been implemented in AM4 (this study) and previously in ACCESS1.0 (Ackerley and Dommenget 2016; Andrews et al. 2021), a key challenge lies in maintaining model stability and physical consistency when decoupling land temperatures from the broader climate system. Modifying model workflows and managing the exchange of information between atmospheric and land components is often highly model specific and may require substantial effort. Nevertheless, when implemented successfully, fixing land temperatures provides a valuable framework for isolating land surface contributions and advancing our understanding of land-driven climate responses.

Acknowledgments. We thank Sergey Malyshev for his comments and suggestions for the initial draft of this work. We thank Tim Andrews, Andrew Williams, and an anonymous reviewer for their insightful comments and suggestions. We also thank Editor Isla Simpson's help during the review process.

Data availability statement. The standard AM4 model code is available at https://github.com/NOAA-GFDL/AM4. Annual-mean outputs of key variables used in this study, such as surface temperature, radiation, and precipitation, can be found at https://zenodo.org/records/15271481.

REFERENCES

Ackerley, D., and D. Dommenget, 2016: Atmosphere-only GCM (ACCESS1.0) simulations with prescribed land surface temperatures. *Geosci. Model Dev.*, **9**, 2077–2098, https://doi.org/10.5194/gmd-9-2077-2016.

——, R. Chadwick, D. Dommenget, and P. Petrelli, 2018: An ensemble of AMIP simulations with prescribed land surface temperatures. *Geosci. Model Dev.*, **11**, 3865–3881, https://doi.org/10.5194/gmd-11-3865-2018.

Alessi, M. J., and M. A. Rugenstein, 2023: Surface temperature pattern scenarios suggest higher warming rates than current projections. *Geophys. Res. Lett.*, **50**, e2023GL105795, https://doi.org/10.1029/2023GL105795.

Andrews, T., C. J. Smith, G. Myhre, P. M. Forster, R. Chadwick, and D. Ackerley, 2021: Effective radiative forcing in a GCM with fixed surface temperatures. *J. Geophys. Res. Atmos.*, **126**, e2020JD033880, https://doi.org/10.1029/2020JD033880.

——, and Coauthors, 2022: On the effect of historical SST patterns on radiative feedback. *J. Geophys. Res. Atmos.*, **127**, e2022JD036675, https://doi.org/10.1029/2022JD036675.

Bloch-Johnson, J., and Coauthors, 2024: The Green's Function Model Intercomparison Project (GFMIP) protocol. *J. Adv. Model. Earth Syst.*, **16**, e2023MS003700, https://doi.org/10.1029/2023MS003700.

Chadwick, R., D. Ackerley, T. Ogura, and D. Dommenget, 2019: Separating the influences of land warming, the direct CO_2 effect, the plant physiological effect, and SST warming on regional precipitation changes. *J. Geophys. Res. Atmos.*, **124**, 624–640, https://doi.org/10.1029/2018JD029423.

Dong, Y., C. Proistosescu, K. C. Armour, and D. S. Battisti, 2019: Attributing historical and future evolution of radiative feedbacks to regional warming patterns using a Green's function

approach: The preeminence of the western Pacific. *J. Climate*, **32**, 5471–5491, https://doi.org/10.1175/JCLI-D-18-0843.1.

Doutriaux-Boucher, M., M. Webb, J. M. Gregory, and O. Boucher, 2009: Carbon dioxide induced stomatal closure increases radiative forcing via a rapid reduction in low cloud. *Geophys. Res. Lett.*, **36**, L02703, https://doi.org/10.1029/2008GL036273.

Forster, P. M., and Coauthors, 2016: Recommendations for diagnosing effective radiative forcing from climate models for CMIP6. *J. Geophys. Res. Atmos.*, **121**, 12 460–12 475, https://doi.org/10.1002/2016JD025320.

Gregory, J. M., and T. Andrews, 2016: Variation in climate sensitivity and feedback parameters during the historical period. *Geophys. Res. Lett.*, **43**, 3911–3920, https://doi.org/10.1002/2016GL068406.

——, and Coauthors, 2004: A new method for diagnosing radiative forcing and climate sensitivity. *Geophys. Res. Lett.*, **31**, L03205, https://doi.org/10.1029/2003GL018747.

Guillaume-Castel, R., and B. Meyssignac, 2025: Quantifying the influence of the sea surface temperature pattern effect on transient global warming. *J. Climate.*, **38**, 3417–3435, https://doi.org/10.1175/JCLI-D-24-0229.1.

Hansen, J., and Coauthors, 2005: Efficacy of climate forcings. *J. Geophys. Res.*, **110**, D18104, https://doi.org/10.1029/2005JD005776.

Haugstad, A., K. Armour, D. Battisti, and B. Rose, 2017: Relative roles of surface temperature and climate forcing patterns in the inconstancy of radiative feedbacks. *Geophys. Res. Lett.*, **44**, 7455–7463, https://doi.org/10.1002/2017GL074372.

Hsieh, T.-L., G. A. Vecchi, C. Wang, W. Yang, B. Zhang, and B. J. Soden, 2024: Dependence of tropical cyclone seeds and climate sensitivity on tropical cloud response. *Sci. Adv.*, **10**, eadi2779, https://doi.org/10.1126/sciadv.adi2779.

Koch, D., T. C. Bond, D. Streets, N. Unger, and G. R. Van der Werf, 2007: Global impacts of aerosols from particular source regions and sectors. *J. Geophys. Res. Atmos.*, **112**, D02205, https://doi.org/10.1029/2005JD007024.

Myhre, G., and Coauthors, 2013: Anthropogenic and natural radiative forcing. *Climate Change 2013: The Physical Science Basis*, T. F. Stocker et al., Eds., Cambridge University Press, 659–740.

——, and Coauthors, 2017: PDRMIP: A Precipitation Driver and Response Model Intercomparison Project, protocol and preliminary results. *Bull. Amer. Meteor. Soc.*, **98**, 1185–1198, https://doi.org/10.1175/bams-d-16-0019.1.

——, R. E. Byrom, T. Andrews, P. M. Forster, and C. J. Smith, 2024: Efficacy of climate forcings in transient CMIP6 simulations. *Front. Climate*, **6**, 1397358, https://doi.org/10.3389/fclim.2024.1397358.

Pincus, R., P. M. Forster, and B. Stevens, 2016: The Radiative Forcing Model Intercomparison Project (RFMIP): Experimental protocol for CMIP6. *Geosci. Model Dev.*, **9**, 3447–3460, https://doi.org/10.5194/gmd-9-3447-2016.

Quan, H., B. Zhang, C. Wang, and S. Fueglistaler, 2024: Nonlinear radiative response to patterned global warming due to convection aggregation and nonlinear tropical dynamics. *J. Climate*, **37**, 5675–5686, https://doi.org/10.1175/JCLI-D-23-0539.1.

——, ——, ——, and ——, 2025: The sea surface temperature pattern effect on outgoing longwave radiation: The role of large-scale convective aggregation. *Geophys. Res. Lett.*, **52**, e2024GL112756, https://doi.org/10.1029/2024GL112756.

Ramaswamy, V., and Coauthors, 2019: Radiative forcing of climate: The historical evolution of the radiative forcing concept, the forcing agents and their quantification, and applications. *A Century of Progress in Atmospheric and Related Sciences: Celebrating the American Meteorological Society Centennial*, *Meteor. Monogr.*, No. 59, Amer. Meteor. Soc., https://doi.org/10.1175/AMSMONOGRAPHS-D-19-0001.1.

Salvi, P., J. M. Gregory, and P. Ceppi, 2023: Time-evolving radiative feedbacks in the historical period. *J. Geophys. Res. Atmos.*, **128**, e2023JD038984, https://doi.org/10.1029/2023JD038984.

Sherwood, S. C., S. Bony, O. Boucher, C. Bretherton, P. M. Forster, J. M. Gregory, and B. Stevens, 2015: Adjustments in the forcing-feedback framework for understanding climate change. *Bull. Amer. Meteor. Soc.*, **96**, 217–228, https://doi.org/10.1175/BAMS-D-13-00167.1.

Smith, C. J., and Coauthors, 2018: Understanding rapid adjustments to diverse forcing agents. *Geophys. Res. Lett.*, **45**, 12 023–12 031, https://doi.org/10.1029/2018GL079826.

——, R. J. Kramer, and A. Sima, 2020a: The HadGEM3-GA7.1 radiative kernel: The importance of a well-resolved stratosphere. *Earth Syst. Sci. Data*, **12**, 2157–2168, https://doi.org/10.5194/essd-12-2157-2020.

——, and Coauthors, 2020b: Effective radiative forcing and adjustments in CMIP6 models. *Atmos. Chem. Phys.*, **20**, 9591–9618, https://doi.org/10.5194/acp-20-9591-2020.

Soden, B. J., I. M. Held, R. Colman, K. M. Shell, J. T. Kiehl, and C. A. Shields, 2008: Quantifying climate feedbacks using radiative kernels. *J. Climate*, **21**, 3504–3520, https://doi.org/10.1175/2007JCLI2110.1.

Stevens, B., S. C. Sherwood, S. Bony, and M. J. Webb, 2016: Prospects for narrowing bounds on Earth's equilibrium climate sensitivity. *Earth's Future*, **4**, 512–522, https://doi.org/10.1002/2016EF000376.

Tang, T., and Coauthors, 2019: Comparison of effective radiative forcing calculations using multiple methods, drivers, and models. *J. Geophys. Res. Atmos.*, **124**, 4382–4394, https://doi.org/10.1029/2018JD030188.

Thompson, D. W., M. Rugenstein, P. M. Forster, and L. Fredericks, 2025: An observational estimate of the pattern effect on climate sensitivity: The importance of the eastern tropical Pacific and land areas. *J. Climate.*, **38**, 4233–4249, https://doi.org/10.1175/JCLI-D-23-0737.1.

Wang, C., W. Yang, G. Vecchi, B. Zhang, B. J. Soden, and D. Chan, 2025: Diagnosing the factors that contribute to the intermodel spread of climate feedback in CMIP6. *J. Climate*, **38**, 663–674, https://doi.org/10.1175/JCLI-D-23-0528.1.

Williams, A. I., N. Jeevanjee, and J. Bloch-Johnson, 2023: Circus tents, convective thresholds, and the non-linear climate response to tropical SSTs. *Geophys. Res. Lett.*, **50**, e2022GL101499, https://doi.org/10.1029/2022GL101499.

Wyant, M. C., C. S. Bretherton, P. N. Blossey, and M. Khairoutdinov, 2012: Fast cloud adjustment to increasing CO_2 in a superparameterized climate model. *J. Adv. Model. Earth Syst.*, **4**, M05001, https://doi.org/10.1029/2011MS000092.

Zhang, B., M. Zhao, and Z. Tan, 2023a: Using a Green's function approach to diagnose the pattern effect in GFDL AM4 and CM4. *J. Climate*, **36**, 1105–1124, https://doi.org/10.1175/JCLI-D-22-0024.1.

——, ——, H. He, B. J. Soden, Z. Tan, B. Xiang, and C. Wang, 2023b: The dependence of climate sensitivity on the meridional distribution of radiative forcing. *Geophys. Res. Lett.*, **50**, e2023GL105492, https://doi.org/10.1029/2023GL105492.

Zhao, M., and Coauthors, 2018a: The GFDL global atmosphere and land model AM4.0/LM4.0: 1. Simulation characteristics with prescribed SSTs. *J. Adv. Model. Earth Syst.*, **10**, 691–734, https://doi.org/10.1002/2017MS001208.

——, and Coauthors, 2018b: The GFDL global atmosphere and land model AM4.0/LM4.0: 2. Model description, sensitivity studies, and tuning strategies. *J. Adv. Model. Earth Syst.*, **10**, 735–769, https://doi.org/10.1002/2017MS001209.

Zhou, C., M. D. Zelinka, and S. A. Klein, 2017: Analyzing the dependence of global cloud feedback on the spatial pattern of sea surface temperature change with a Green's function approach. *J. Adv. Model. Earth Syst.*, **9**, 2174–2189, https://doi.org/10.1002/2017MS001096.